Nanoscale

PAPER

View Article Online
View Journal | View Issue

Cite this: *Nanoscale*, 2015, **7**, 8782

Superior plasmon absorption in iron-doped gold nanoparticles†

Vincenzo Amendola,*[a] Rosalba Saija,[b] Onofrio M. Maragò[c] and Maria Antonia Iatì[c]

Received 4th February 2015,
Accepted 8th April 2015

DOI: 10.1039/c5nr00823a

www.rsc.org/nanoscale

Although the excitation of localized surface plasmons is associated with enhanced scattering and absorption of incoming photons, only the latter is relevant for the efficient conversion of light into heat. Here we show that the absorption cross section of gold nanoparticles is sensibly increased when iron is included in the lattice as a substitutional dopant, *i.e.* in a gold–iron nanoalloy. Such an increase is size and shape dependent, with the best performance observed in nanoshells where a 90–190% improvement is found in a size range that is crucial for practical applications. Our findings are unexpected according to the common belief and previous experimental observations that alloys of Au with transition metals show a depressed plasmonic response. These results are promising for the design of efficient plasmonic converters of light into heat and pave the way to more in-depth investigations of the plasmonic properties in noble metal nanoalloys.

Introduction

Multiple scientific and technological applications rely on localized surface plasmon resonances (LSPRs), which occurs when free electrons in nanoparticles (NPs) are collectively excited by electromagnetic radiation.[1] The highest values known in nature for the extinction cross section (σ_{Ext}) are found in noble metal NPs.[2] Photons exciting plasmons are either absorbed or scattered, and the probability of the two events is determined, respectively, by the NP absorption (σ_{Abs}) and scattering (σ_{Sca}) cross sections, whose sum gives the σ_{Ext}.[3,4] Since different properties are associated with scattering and absorption, σ_{Abs} and σ_{Sca} are the relevant quantities for real applications of plasmonic NPs.[5–7] Light scattering is an elastic process consisting in the modification of photon propagation direction,[3] therefore NPs with a large σ_{Sca} are preferentially exploited for biolabelling and sensing up to single particle sensitivity,[8] as well as for nanolensing and enhancement of nonlinear optical properties in nearby objects,[9–13] such as plasmonic enhanced near-field absorption in solar cells,[14] surface enhanced Raman scattering[15–17] or plasmonic enhanced third harmonic generation.[18]

Instead, light absorption consists in the transfer of photon energy to the plasmonic nanostructure, where it is rapidly converted to heat.[7] Therefore, NPs with a large σ_{Abs} are suitable for photothermal processes such as photothermal therapy,[6,19,20] drug release,[21,22] photoacoustic imaging[8,23] photothermal contrast imaging,[24,25] photothermal-induced resonance imaging,[26] photothermal polymerization,[27] plasmonic patterning[28,29] and light induced vapour generation.[30–32] Another consequence of photon absorption is the alteration of the equilibrium electron Fermi distribution in the metal NPs,[33–35] which allows charge injection in the conduction band of nearby semiconductors[33,36] and it is exploited for plasmon-enhanced catalysis[37,38] and photocurrent generation.[39,40]

Since the σ_{Abs} and σ_{Sca} of noble metal NPs grow with, respectively, the 3rd and 6th power of particle size,[3,6] there is a size threshold at which scattering equals absorption.[5,6] This threshold depends on the shape, structure, and composition of NPs,[6,41] and for noble metal NPs it falls approximately at 60–100 nm.[6,42,43] Consequently, absorption for unit mass is maximized by reducing the particle size,[42,43] although in this way the absolute capacity of light-to-heat conversion in the single NP is dramatically diminished.[5,6,42,44] Alternatively, one can choose the shape and structure to maximize the absorption cross section.[5,6,20] For instance, at equal volumes, Au nanorods (NRs) have larger σ_{Abs} than Au nanoshells (NSs) composed of a silica core coated with a gold layer.[5,6]

In addition to the size and structure, the composition of metal NPs is another degree of freedom to maximize the plasmon absorption.[9] This controls the complex permittivity, ε, on which σ_{Abs} and σ_{Sca} ultimately depends.[1,3] Indeed, composition has been seldom considered as a parameter for tuning the plasmonic response of noble metal NPs,[9,45–49] and

[a]*Department of Chemical Sciences, University of Padova, via Marzolo 1, I-35131 Padova, Italy. E-mail: vincenzo.amendola@unipd.it*
[b]*Dipartimento di Fisica e di Scienze della Terra, Università di Messina, v.le F. Stagno D'Alcontres 31, I-98166 Messina, Italy*
[c]*CNR-IPCF, Istituto per i Processi Chimico-Fisici, v.le F. Stagno D'Alcontres 37, I-98158 Messina, Italy*

†Electronic supplementary information (ESI) available: Definition of σ[400–1200 nm] and σ(800 nm), spectral dependence of σ_{Abs}, experimental AuFe optical constants. See DOI: 10.1039/c5nr00823a

there is a relatively low number of metal plasmonic nanoparticles composed of elements different from Au or Ag, such as Pt,[50] Pd,[51] Ga[52] or Al.[53] This is often motivated by the general assumption that other metals cannot perform better than pure Au and Ag nanostructures, either in terms of plasmonic response, ease of synthesis, physical–chemical stability or biocompatibility.[2,45]

However, recent interest in magneto-plasmonics[48,54–56] and plasmon enhanced catalysis[57,58] led beyond the well known Au and Ag nanostructures, to the synthesis of plasmonic nanoalloys, such as Au–Fe,[48,54] Au–Pt[58] and Au–Pd[57] compounds. In these nanosystems, the plasmonic performance strongly depends on the alloy composition and stoichiometry. In fact, alloying induces the modification of the band structure of the original metals, *e.g.*, by changing the optical gap, moving the Fermi energy and introducing new interband transitions.[45] In general, these alloys exhibit σ_{Ext} and local field enhancement inferior to pure noble metals with identical size and shape,[48,54,57,58] which explains the modest number of studies in which these systems are used purely for plasmonic applications.

Here, we show that the alloy NPs composed of a noble metal (Au) doped with 5–15 atomic% (at%) of a transition metal (Fe) have superior absorption cross section to the pure Au counterparts. We started from the experimentally measured optical constants of Au–Fe alloys,[59] in which iron is present as a substitutional dopant in the face centered cubic lattice of gold, to calculate by analytical (Mie theory) and numerical (Discrete Dipole Approximation) methods the dependence of plasmon cross sections on the size and shape of nanostructures. The augmented plasmon absorption in iron-doped Au nanoalloys is prevalently observed in the red and near infrared (NIR) frequencies, which actually is the working window for most photothermal applications.[5,8] In general, these results suggest that the scarcely investigated field of plasmonic nanoalloys can be a source of new, yet unforeseen solutions for the improvement of plasmonic performance.

Results

Iron-doped gold nanoshells

As a benchmark material for photothermal applications, we first considered Au NSs.[60] In synthetic Au NSs, the scattering cannot be minimized simply by reducing the size of the whole nanostructure, due to experimental difficulties in the control of the thickness of the metal layer.[5,60] In fact, to obtain a plasmon resonance peaked in the red or NIR, as required in most biological applications of NSs,[8,60] the gold layer must be small compared to the silica core, and ordinary synthetic approaches usually do not allow a thickness below *ca.* 10 nm, unless porous hollow nanostructures such as Au nanocages are preferred.[61] As a consequence, the literature usually reports the use of NSs with a size above 100 nm,[19,21,31,32,62,63] whose heating performance is severely limited by the large scattering contribution.[5,6,64] Increasing the σ_{Abs} by acting only on the composition of the metal layer, while maintaining unaltered NS shape and size, would be the preferential strategy to improve the photothermal features of these nanomaterials.[6,60,63] Besides, recent studies evidenced that multiple scattering in NSs is useful to concentrate light absorption in very small volumes.[65]

Therefore, by means of Mie theory, we calculated the dependence of σ_{Ext}, σ_{Abs} and σ_{Sca} on the composition of Fe-doped Au alloys, considering a NS with a SiO_2 core of radius 60 nm and a 16 nm thick metal shell (60, 16), inspired by those often described in the literature for photothermal applications (Fig. 1).[60,63,66] In order to quantitatively compare the plasmo-

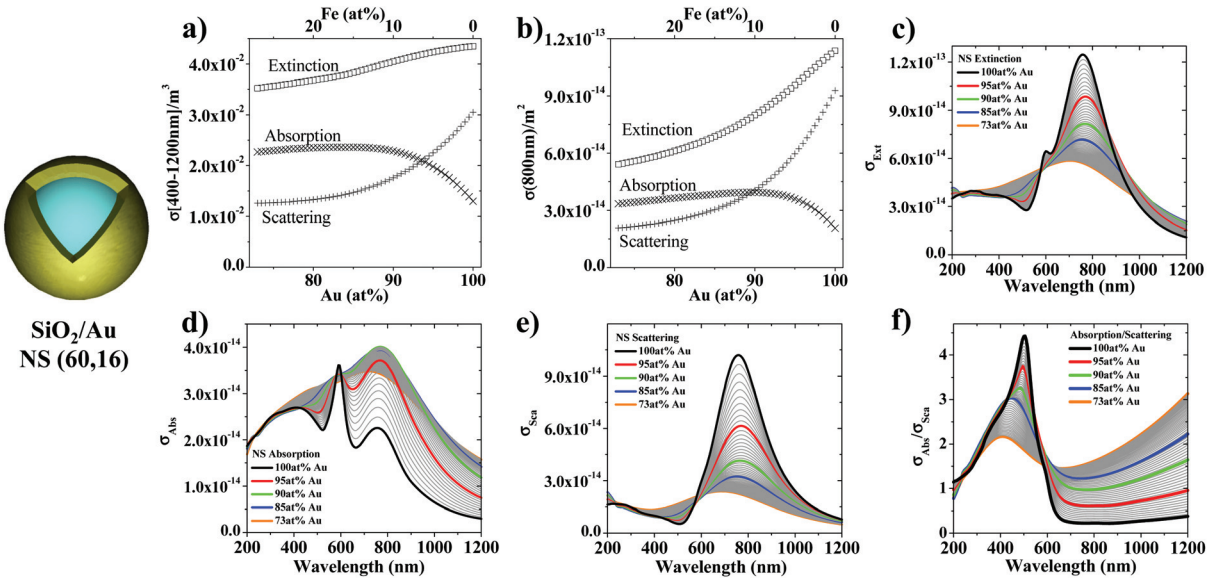

Fig. 1 Mie theory calculations of a (60, 16) NS in water *versus* iron doping. (a) σ_{Ext} [400–1200 nm], σ_{Abs} [400–1200 nm] and σ_{Sca} [400–1200 nm]. (b) σ_{Ext} (800 nm), σ_{Abs} (800 nm) and σ_{Sca} (800 nm). (c–f) Spectral dependence of σ_{Ext} (c), σ_{Abs} (d), σ_{Sca} (e) and $\sigma_{Abs}/\sigma_{Sca}$ (f).

nic performance as a function of iron doping, in Fig. 1a we show the integrated extinction, absorption and scattering cross sections in the 400–1200 nm spectral range (σ_{Ext} [400–1200 nm], σ_{Abs} [400–1200 nm] and σ_{Sca} [400–1200 nm], respectively, see also Fig. S1 in the ESI†), which is the interval where LSPR of NSs is typically observed.[60] The plot of σ_{Ext} [400–1200 nm] has a maximum for 100 at% Au, whereas extinction decreases with increasing Fe content, as expected from the literature.[48,54] However, by looking at the two contributions to σ_{Ext} originating from absorption and scattering, we found that σ_{Sca} and σ_{Abs} have two opposite trends. The σ_{Sca} steeply decreases with the Fe content, reaching a plateau at 40% of the pure Au value when iron exceeds 25 at%. Instead, the plot of σ_{Abs} shows a remarkable maximum corresponding to 182% of its initial value in proximity to 15 at% of iron, and it is always larger than that in the pure Au NS. A similar trend is observed in the plot of the σ_{Ext}, σ_{Abs} and σ_{Sca} values calculated at 800 nm (Fig. 1b), which is the wavelength frequently exploited for *in vivo* photothermal applications.[8,60] In this case, the maximum of σ_{Abs} (800 nm) is close to 10 at% of iron, where an increase of the 190% of the value in pure Au NS is observed. The spectral profiles of σ_{Ext}, σ_{Abs} and σ_{Sca} are compared in Fig. 1c–e, showing that the plasmon resonance broadens for increasing Fe doping, in agreement with the recently observed plasmon damping in spherical Au–Fe alloy NPs with different compositions.[48,54] Interestingly, from the $\sigma_{Abs}/\sigma_{Sca}$ ratio reported in Fig. 1f, one can see that the absorption markedly dominates over scattering in doped Au NSs when the wavelength is longer than 600 nm, whereas below this wavelength the trend is inverted and the absorption over the scattering ratio is larger in pure Au NSs.

In order to confirm the generality of our finding, we calculated the integrated σ_{Abs} [400–1200 nm] and the σ_{Abs} (800 nm) for a series of NSs with structural parameters extracted from the literature[19,21,31,32,60,62,63,66] (Fig. 2a–b and S2 in the ESI†), focusing on four representative levels of iron doping (0, 5, 10 and 15 at% Fe). We found that the calculated plasmon absorption is systematically larger in the doped Au nanostructures, with an improvement reaching a remarkable +190% in the (60, 22) NSs. Such an increase of σ_{Abs} can prove useful to minimize damage of healthy tissues in photothermal therapy,[60] as well as to increase the minimum detectable amount of NSs in photothermal imaging techniques.[63] In general, such an improvement would allow the reduction of the dose of nanomaterials administered for theragnostic purposes, which is important for the minimization of side effects related to long term accumulation of the nanodrugs.[60,63]

Since (60, 12) NSs have also been applied to vapour generation by conversion of sunlight into heat,[30–32] the more appropriate parameter to evaluate the photothermal performance for such a specific application is the convolution of the solar spectral irradiance at air mass 1.5 (AM1.5) with σ_{Abs}.[30–32] In this case (see Fig. 2c), a remarkable improvement of 40% in the light-to-heat conversion is predicted in the 280–1200 nm wavelength range by doping the Au shell with 10 at% of Fe.

In Fig. 2d–g we further investigated the effect of Fe doping as a function of the structural parameters of NSs, such as the size and shell thickness (see also Fig. S3–S4†). When the shell thickness exceeds 10 nm, the σ_{Abs} [400–1200 nm] and the σ_{Abs} (800 nm) of doped shells surmount by more than 50% those of pure Au NSs for increasing shell thickness and a fixed diameter of 140 nm (Fig. 2d–e and S3†). As stated before, this is equivalent to the smallest thickness found in the literature.[60] Interestingly, when σ_{Abs} [400–1200 nm] is plotted *versus* NS diameter (Fig. 2f), while maintaining the ratio of core-to-shell thickness at 4 : 1 unaltered, we observe that iron-doped NSs have superior absorption only when the size exceeds the threshold value of 100 nm. A different behaviour is observed for the value of σ_{Abs} at 800 nm (Fig. 2e), which is larger in Fe-doped NSs in the whole range of diameters considered, with an increase of +50% already for a size of 70 nm. Indeed, the spectral profiles of σ_{Abs} (Fig. S4 in the ESI†) show increasing bandwidth for increasing Fe-doping, which is the main reason for the superior σ_{Abs} (800 nm) of doped NSs with the size below 100 nm, but only above this threshold the σ_{Abs} of alloy NSs becomes larger than pure Au NSs in the whole red-NIR spectral range.

Role of shape: spheres, dimers, and nanorods

The effect of iron-doping was investigated further by considering other shapes exploited for photothermal applications, such as compact spheres, sphere dimers and nanorods (Fig. 3 and S5–S8 in the ESI†). In the case of compact spheres, the plot of σ_{Abs} [400–1200 nm] *versus* size for the four representative levels of iron-doping reported in Fig. 3a shows that Au–Fe NPs absorb 100% more than Au NPs when particles are bigger than 100 nm. The σ_{Abs} (800 nm) of the alloy is larger than that in Au NPs in the whole range of size considered (Fig. 3b), although this is again related to the plasmon bandwidth in doped particles with a diameter below 70 nm (see Fig. S5 in the ESI†). Instead, the σ_{Abs} of alloys becomes superior in the whole spectral range only for sizes exceeding 70 nm.

Surprisingly, the beneficial effect of iron doping on plasmon absorption is less conspicuous in a dimer of spheres separated by a 1 nm gap (Fig. 3c–d). The plot of σ_{Abs} [400–1200 nm] *versus* sphere's diameter shows a maximum increment of +30% for 140 nm alloys, with only a slight increment when the iron-doped nanospheres exceed 70 nm (Fig. 3c and S6a†). The trend of σ_{Abs} (800 nm) reflects that of monomers (Fig. 3d), with the best absorption increment (+80%) observed in Au–Fe dimers larger than 100 nm, whereas the behaviour at lower size is dominated by the dependence of plasmon bandwidth on iron-doping (see Fig. S6b–h in the ESI†).

The case of NRs with hemispherical caps can help obtaining more insights about the difference between isolated and coupled nanospheres (Fig. 3e–h and S7–S8†). In fact, NRs have elongated shape and plasmon resonances in the red and NIR,[6] similarly to sphere's dimers. At the same time, isolated NRs are not subjected to the enormous local field enhancement

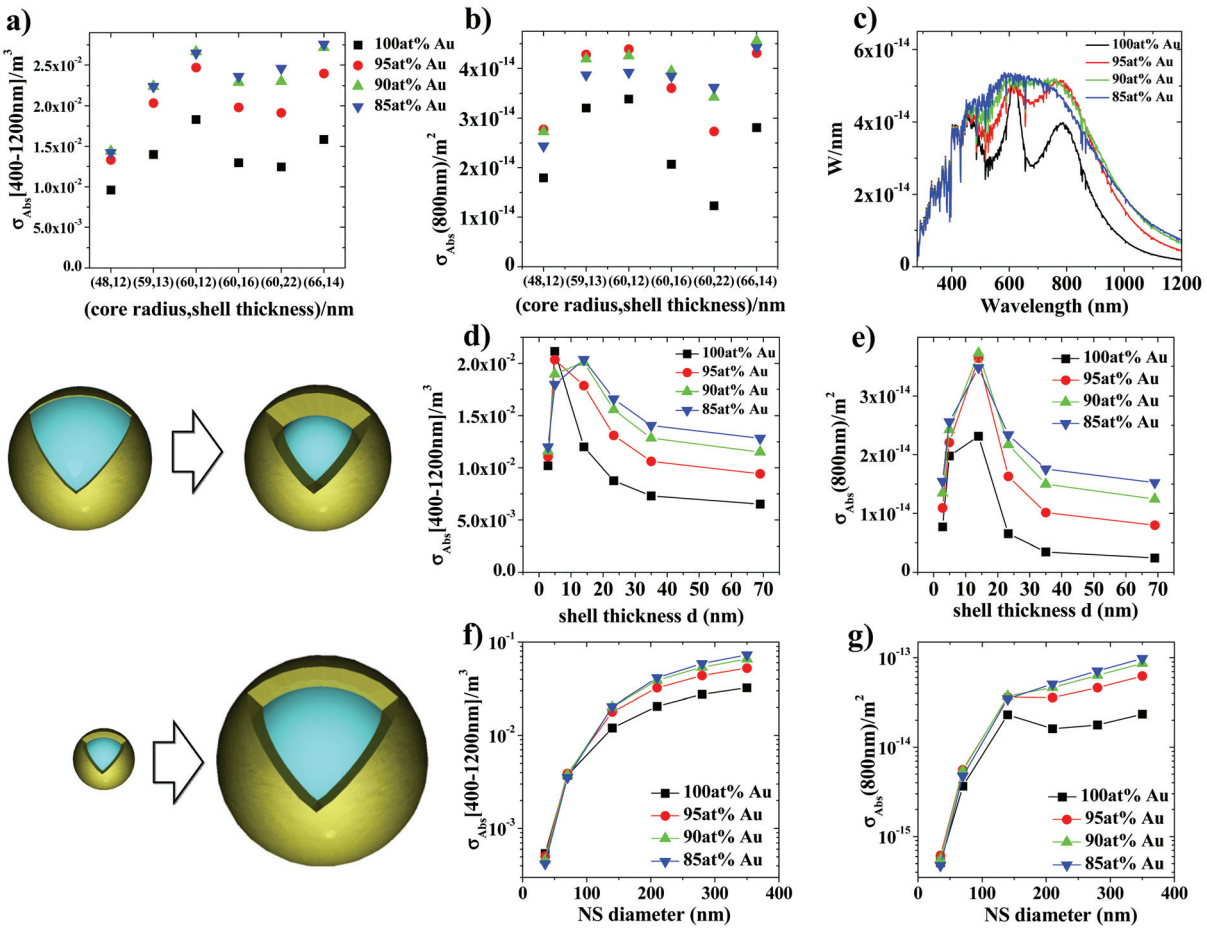

Fig. 2 σ_{Abs} [400–1200 nm] (a) and σ_{Abs} (800 nm) (b) for four representative levels of iron doping (0 at% Fe–100 at% Au in black squares, 5 at% Fe–95 at% Au in red circles, 10 at% Fe–90 at% Au in green triangles, 15 at% Fe–85 at% Au in blue triangles) in a series of NSs with structural parameters extracted from the literature (for details see the text). (c) Convolution of σ_{Abs} with the solar spectral AM1.5 irradiance. (d, e) Variation of σ_{Abs} [400–1200 nm] (d) and σ_{Abs} (800 nm) (e) in a NS with a constant diameter of 140 nm and variable shell thickness. (f, g) Variation in σ_{Abs} [400–1200 nm] (f) and σ_{Abs} (800 nm) (g) in a NS with a constant ratio of core to shell of 4 : 1 and variable diameters.

typically observed at the hot spots in the junction between two plasmonic nanospheres.[15] For an easier comparison of NRs with nanospheres, dimers and NSs, we considered the effective size d_{eff}, defined as the diameter of the equivolume sphere.[6,43] In the case of a NR with a major to minor axis ratio (aspect ratio) of 2.5 and incident electric field polarized along the major axis, we found that the σ_{Abs} [400–1200 nm] of Au–Fe alloys is up to 150% larger than that in pure Au when d_{eff} is larger than 70 nm (Fig. 3e and S7†). Similarly, σ_{Abs} (800 nm) of iron-doped NRs exceeds by 70–380% that of pure Au rods (Fig. 3f).

To better elucidate the influence of the shape on the absorption performance of iron-doped alloys, we also investigated the effect of the rod's aspect ratio in the range from 1.5 to 5.5, while maintaining unchanged d_{eff} at 110 nm. For the whole range of aspect ratios, doped NRs have superior absorption performance (Fig. 3g–h and S8†), suggesting that the particle geometry is less important than size.

Discussion

Overall, our calculations show that plasmon absorption is sensibly improved in iron-doped Au nanostructures larger than 70–100 nm. Below this size threshold, the benefits of iron doping on the σ_{Abs} are minimal and prevalently observed in the NIR as a consequence of plasmonic band broadening in Au–Fe alloy NPs. The change of σ_{Abs} originates from the modification of the optical constants of gold after doping with iron. Previous experimental studies on the optical properties of thin AuFe alloy films[59] and nanospheres[48,54] showed that doping Au with Fe introduces new single electron transitions, which are generated by electrons lying in the iron d-states below the Fermi surface of the metal. In general, low-frequency interband transitions are observed when noble metals and transition metals with partially occupied d-states are alloyed together.[45,59,67] These low-energy transitions favour the rapid decay of the plasmon excitation into electron–hole pairs,[45]

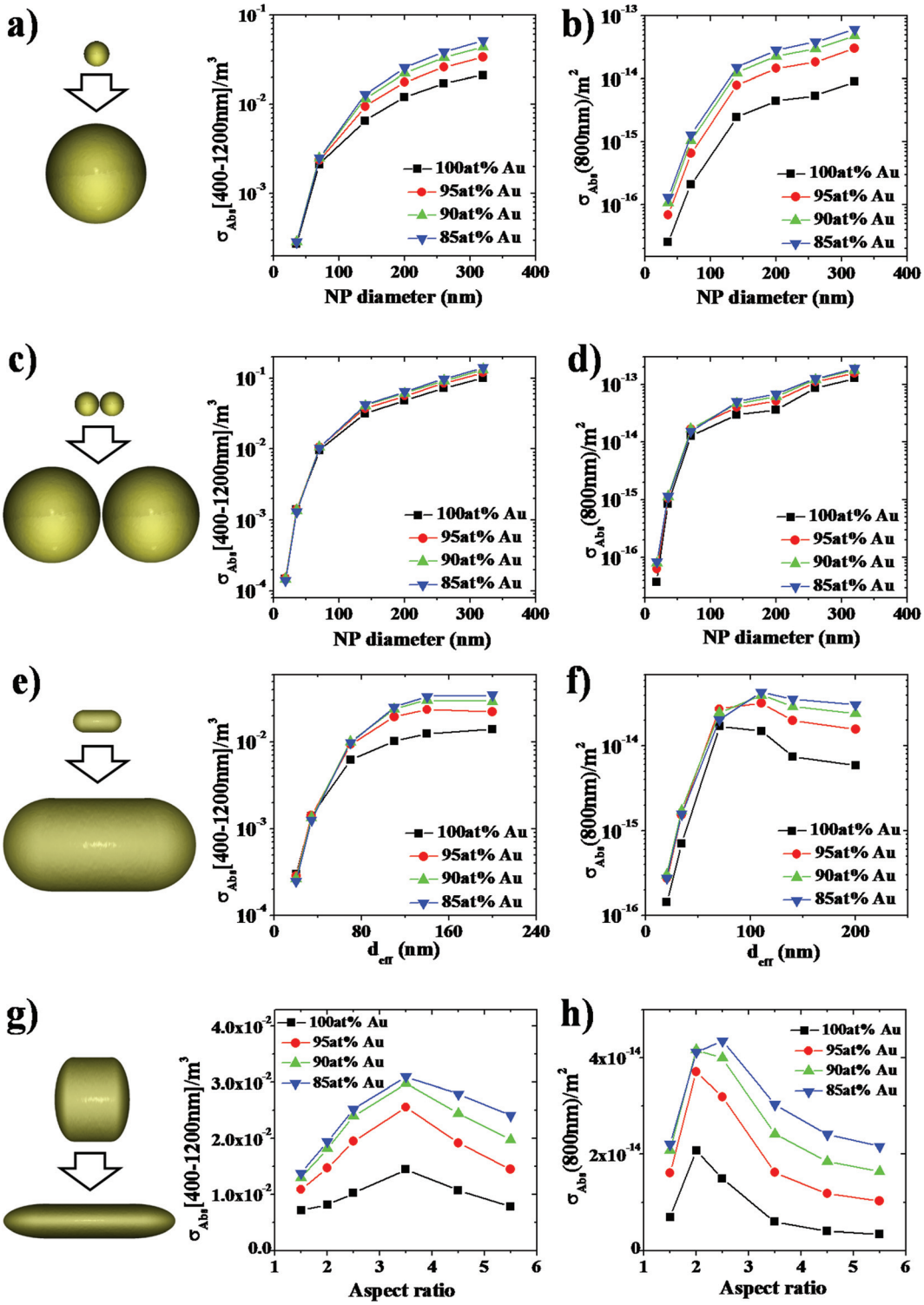

Fig. 3 (a, b) σ_{Abs} [400–1200 nm] (a) and σ_{Abs} (800 nm) (b) in nanospheres with different sizes. (c, d) σ_{Abs} [400–1200 nm] (c) and σ_{Abs} (800 nm) (d) in a dimer of nanospheres with different sizes and an interparticle gap of 1 nm. (e, f) σ_{Abs} [400–1200 nm] (e) and σ_{Abs} (800 nm) (f) in NRs with the aspect ratio of 2.5 and different effective sizes. (g, h) σ_{Abs} [400–1200 nm] (g) and σ_{Abs} (800 nm) (h) in NRs with variable aspect ratios and a constant effective size of 110 nm.

thus being the main cause for plasmon band broadening in Au–Fe alloys.[48,54] This effect increases with the concentration of the transition metal in the alloy.[48,59] Moreover, Fe has a smaller atomic number than Au, meaning that the overall electronic structure of the alloy is different compared to pure Au.[45,59,68] For these reasons, iron doping modifies the band

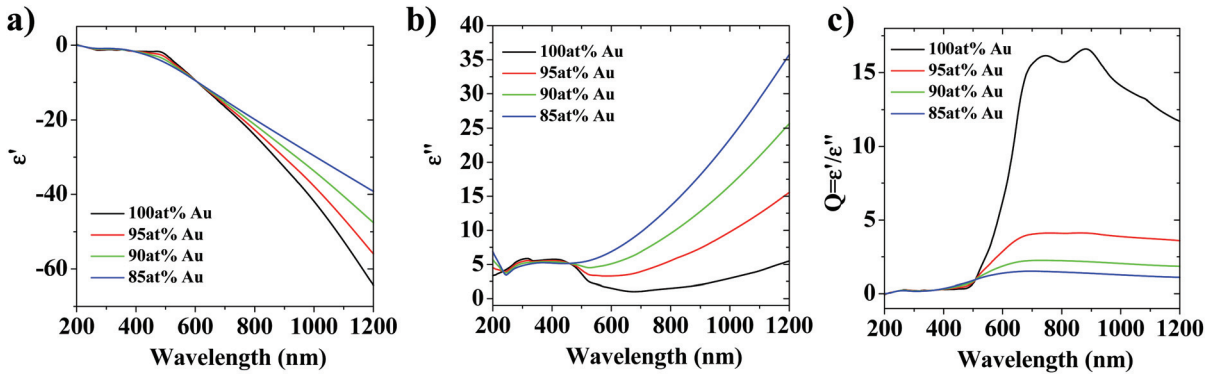

Fig. 4 Real (a) and imaginary (b) parts of the optical constant for four representative levels of iron doping (0 at% Fe–100 at% Au in black, 5 at% Fe–95 at% Au in red, 10 at% Fe–90 at% Au in green, 15 at% Fe–85 at% Au in blue). (c) The plasmonic quality factor Q for the same four compositions.

structure of the metal and the resulting optical permittivity, in particular by decreasing its real component (ε') and increasing its imaginary part (ε'') in comparison with pure Au (see Fig. 4a–b).

The effect of iron-doping on the plasmonic absorption of Au nanostructures can be explained by considering the dependence of σ_{Abs} for a generic NP at the photon frequency ω:[43,69,70]

$$\sigma_{Abs}(\omega) = \frac{k}{\varepsilon_0 |E_0|^2} \varepsilon'' \int_{NP} |E_{NP}|^2 dV_{NP} \quad (1)$$

where E_0 is the electric field of the incident light, measured in the medium surrounding the NP of volume V_{NP}, ε_0 is the vacuum dielectric permittivity and E_{NP} is the electric field of the electromagnetic radiation inside the NP. On the one hand, $\sigma_{Abs}(\omega)$ is proportional to the lossy part of the optical constant ε'', which is augmented by iron doping (see Fig. 4b). On the other hand, $\sigma_{Abs}(\omega)$ is proportional to the square of the electric field E_{NP} inside the NP, which is maximized when the quality factor Q of the plasmon resonance is maximum.[69,70] Following Blaber,[70] the plasmonic performance of metals with different compositions can be compared, independent of the particle geometry, assuming that $Q = -\varepsilon'/\varepsilon''$. In Fig. 4c we report Q for the same four representative Au–Fe compositions of Fig. 2–3, and we clearly found that Q is largest in pure Au. This is in agreement with the fact that highest σ_{Ext} is systematically obtained for Au NPs rather than Au–Fe alloys (see, *e.g.*, Fig. 1). Therefore, iron doping has the two opposite effects of increasing ε'' and decreasing E_{NP}, and the Au–Fe alloys have superior σ_{Abs} only when the ε'' contribution prevails over $|E_{NP}|^2$ in eqn (1). It is important to point out that, in addition to composition, E_{NP} depends also on the particle shape, size and assembly,[70] and it is not uniform throughout the NP volume.[45,71] In particular, the value of E_{NP} in proximity to small gaps in assemblies of nanoparticles is several orders of magnitude larger than that in isolated nanoparticles.[69,70] Indeed, the gaps between NPs are also called hot spots because of such strong electromagnetic field enhancement,[15] and this is the region where the conversion of light into heat is maximum.[69,71] In order to further investigate this point, we calculated, using the multipole field expansion,[4,72,73] the internal electric field and mapped $|E_{NP}|^2$ in spheres (Fig. 5a), nanoshells (Fig. 5b) and sphere dimers (Fig. 5b) at the wavelength where plasmon absorption is maximum. In particular, we compared the two opposite cases of pure Au and Au(85)Fe(15) NPs and we considered two distinct sizes corresponding to the spheres with diameters of 35 nm and 140 nm, *i.e.* below and above the threshold for the amplification of plasmon absorption in iron doped NPs. The results confirm that $|E_{NP}|^2$ is always larger in pure Au NPs than in the Fe–Au alloy, although the difference is more evident for 35 nm NPs and for dimers of nanospheres. Besides, one must observe that the maximum of absorbance red shifts for increasing NPs' size, moving to the region where ε'' of the alloy is larger and can compensate the loss in the $|E_{NP}|^2$ term. These two trends explain why the superior plasmon absorption is observed in isolated NPs with the size above ~70 nm such as NSs, nanospheres and NRs, rather than in a dimer of spheres or NPs with the size below ~70 nm, where E_{NP} is the dominant contribution.[15] We expect this trend to be general for all the shapes where the local field enhancement is remarkable, such as in all the coupled nanostructures and particles with sharp tips, corners or edges.

For what concerns the role played by the type of dopant in the Au alloy, a quantitative comparison with other transition elements would be possible by using the experimentally measured optical constants of each compound, as done for the AuFe system in a range of compositions.[48,54,59] However, these data are available only for a limited number of Au alloys containing other noble metals such as Ag, Cu, Pt or Pd,[74] for which no absorption enhancement has been observed in the past.[9,45] In all the other cases, the synthesis of the alloy and the ellipsometric investigation of the optical constants as a function of the composition would be necessary to foresee the plasmonic properties. In fact, as shown in Fig. S10 of the ESI,† the extrapolation of optical constants of alloys from that of pure metals in the absence of an experimental checkpoint is unreliable. However, we know from the literature that the elec-

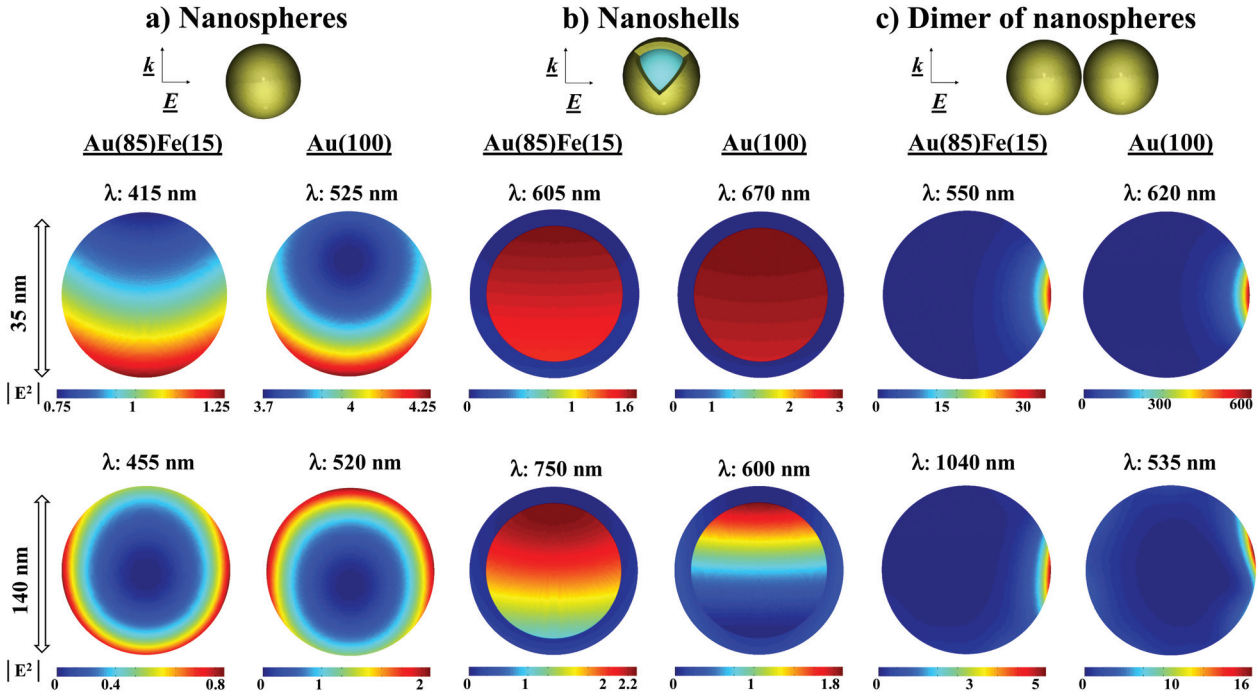

Fig. 5 Map of the internal electric field $|E|^2$ in nanostructures of different shapes (a: nanospheres; b: nanoshells; c: dimer of nanospheres), composition (pure Au or Au(85)Fe(15)), and diameter (35 nm or 140 nm). Calculations are performed for incident monochromatic radiation at the wavelength where the maximum absorption occurs (as indicated in the figure). The incident electric field of the electromagnetic radiation is parallel to the plane of the map. Due to the symmetry of the dimer of nanospheres, only the left side particle is shown.

trons lying in the d-states of Fe dopants below the Fermi level play a major role in the modification of the AuFe alloy band structure, by enabling low-frequency interband transitions.[59,67] On the basis of similar observations on the band structure of other Au alloys,[45,75] we expect that an increased plasmon absorption may also be possible by doping Au with other transition metals with partially filled d-orbitals such as, for instance, Cr, Co and, to a lower extent, Ni. In the case of transition metals such as Pd or Pt, whose d-orbitals are almost (Pd) or completely (Pt) occupied, no such a modification of the Au band structure has been observed in the red or NIR.[76–79] Conversely, an increased absorbance in the UV-visible range due to single-electron transitions from d-states in Pt and Pd and a simultaneous damping of plasmon absorption have been reported.[45,57,58,76–79] This can be explained with the decrease of the real part (ε') of the optical constant of the alloy containing Pd or Pt, and a modest increase of its imaginary part (ε'') at visible frequencies, compared to pure Au.[45,80] In general, this suggests that elements with the occupied d-states are not suitable for the increase of plasmon absorption in Au alloys.

Conclusion

In summary, we showed that iron-doped Au nanostructures with the size above 70–100 nm have superior absorption cross section than the pure Au counterparts. In particular, a remarkable increase of 90–190% is predicted in NSs and nanospheres commonly exploited for photothermal applications. The effect is explained with the modification of the band structure of gold after doping with iron, with consequent increase of the lossy part of the optical constant. These results in general suggest that the band structure of noble metals can be engineered by doping with the appropriate combination of transition metals to obtain the optimized plasmonic properties. At the moment, the optical constants of noble metal alloys containing one or more transition metals are in large part unknown, therefore the real potential of doping for the improvement of plasmonic performance is unexplored, and other transition metals, amongst those miscible with Au, could perform better than iron. Overall, this study fosters interest in the scarcely investigated field of noble metal nanoalloys, which can be a source of new unforeseen solutions for the improvement of plasmonic performance.

Methods

Mie theory for compact spheres

The extinction, scattering and absorption cross-sections of spherical nanoparticles (σ_{Ext}, σ_{Sca} and σ_{Abs}) were calculated using the Mie model for compact spheres:[1,3]

$$\sigma_{Ext} = \frac{2\pi}{|\vec{k}^2|}\sum_{L=1}^{\infty}(2L+1)\mathrm{Re}[a_L + b_L] \qquad (m1)$$

$$\sigma_{\mathrm{Sca}} = \frac{2\pi}{\left|\bar{k}^2\right|}\sum_{L=1}^{\infty}(2L+1)\left(|a_L|^2+|b_L|^2\right) \quad \text{(m2)}$$

$$\sigma_{\mathrm{Abs}} = \sigma_{\mathrm{Ext}} - \sigma_{\mathrm{Sca}} \quad \text{(m3)}$$

$$a_L = \frac{m\cdot\psi_L(mx)\cdot\psi_L'(x) - \psi_L'(mx)\cdot\psi_L(x)}{m\cdot\psi_L(mx)\cdot\eta_L'(x) - \psi_L'(mx)\cdot\eta_L(x)} \quad \text{(m4)}$$

$$b_L = \frac{\psi_L(mx)\cdot\psi_L'(x) - m\psi_L'(mx)\cdot\psi_L(x)}{\psi_L(mx)\cdot\eta_L'(x) - m\psi_L'(mx)\cdot\eta_L(x)} \quad \text{(m5)}$$

$$m = \frac{n(R)}{n_{\mathrm{m}}} \quad \text{(m6)}$$

$$x = |\bar{k}|R, \quad \text{(m7)}$$

where R is the sphere radius, k is the incident photon wave vector in the host matrix with the refractive index n_{m}, Ψ_L and η_L are the spherical Riccati–Bessel functions, and $n(R)$ is the complex refractive index of the sphere. In all calculations, the highest multipolar order (L) considered was 3 and n_{m} = 1.334 (water matrix).

Mie theory for core–shell spheres

The extinction, scattering and absorption cross-sections of NSs were calculated using the generalization of the Mie model for multilayered spheres:[1]

$$\sigma_{\mathrm{Ext}} = \frac{2\pi}{\left|\bar{k}_h{}^2\right|}\sum_{L=1}^{\infty}(2L+1)\mathrm{Re}[a_L+b_L] \quad \text{(m8)}$$

$$\sigma_{\mathrm{Sca}} = \frac{2\pi}{\left|\bar{k}_h{}^2\right|}\sum_{L=1}^{\infty}(2L+1)\left(|a_L|^2+|b_L|^2\right) \quad \text{(m9)}$$

$$\sigma_{\mathrm{Abs}} = \sigma_{\mathrm{Ext}} - \sigma_{\mathrm{Sca}} \quad \text{(m10)}$$

$$m_s = \frac{n_{s+1}}{n_s} \quad \text{(m17)}$$

$$x_s = |\bar{k}_s|R_s \quad \text{(m18)}$$

where $\chi(x)$ is one of the spherical Riccati–Bessel functions, k_{h} is the wavenumber of the incident photons calculated in the host matrix, and s is the layer number, ranging from 1 (the core) to r + 1 (the surrounding matrix with the refractive index n_{m}), with r being the total number of layers (1 in the Au NS case). In all calculations, the highest multipolar order (L) considered was 3 and $n_{s+1} = n_{\mathrm{m}}$ = 1.334 (water matrix).

Maps of internal fields

The maps of the internal electric field intensity, $|E_{\mathrm{NP}}|^2$, in nanospheres, nanoshells, and dimers of nanospheres are obtained through the solutions of the same boundary condition equations defining the Mie expansion coefficients. For the case of dimers, we used the addition theorem for vector spherical harmonics[72] that enables the solution of the scattering problem also for clusters of any size, shape, and composition and the retrieval of the relevant amplitudes for scattered and internal fields.[4,73]

Discrete-dipole approximation method

Calculations of the extinction cross sections of nanosphere dimers and NRs were performed by the DDA method.[81] In DDA, the structure of interest, usually called "target", is composed of a cubic array of N polarizable points (*i.e.* N cubic dipoles). The polarization P_j induced on each dipole j of position r_j and polarizability p_j is given by[81]

$$\overline{P_j} = p_j\overline{E}_{\mathrm{Loc}}(\overline{r}_j) \quad \text{(m19)}$$

$$a_L = \frac{m_r\cdot\psi_L(m_rx_r)\cdot\left[\psi_L'(x_r)+T_L^r\chi_L'(x_r)\right] - \psi_L'(m_rx_r)\cdot\left[\psi_L(x_r)+T_L^r\chi_L(x_r)\right]}{m_r\cdot\eta_L(m_rx_r)\cdot\left[\psi_L'(x_r)+T_L^r\chi_L'(x_r)\right] - \eta_L'(m_rx_r)\cdot\left[\psi_L(x_r)+T_L^r\chi_L(x_r)\right]} \quad \text{(m11)}$$

$$b_L = \frac{\psi_L(m_rx_r)\cdot\left[\psi_L'(x_r)+S_L^r\chi_L'(x_r)\right] - m_r\cdot\psi_L'(m_rx_r)\cdot\left[\psi_L(x_r)+S_L^r\chi_L(x_r)\right]}{\eta_L(m_rx_r)\cdot\left[\psi_L'(x_r)+S_L^r\chi_L'(x_r)\right] - m_r\cdot\eta_L'(m_rx_r)\cdot\left[\psi_L(x_r)+S_L^r\chi_L(x_r)\right]} \quad \text{(m12)}$$

$$T_L^s = -\frac{m_s\cdot\psi_L(m_sx_s)\cdot\left[\psi_L'(x_s)+T_L^{s-1}\chi_L'(x_s)\right] - \psi_L'(m_sx_s)\cdot\left[\psi_L(x_s)+T_L^{s-1}\chi_L(x_s)\right]}{m_s\cdot\chi_L(m_sx_s)\cdot\left[\psi_L'(x_s)+T_L^{s-1}\chi_L'(x_s)\right] - \chi_L'(m_sx_s)\cdot\left[\psi_L(x_s)+T_L^{s-1}\chi_L(x_s)\right]} \quad \text{(m13)}$$

$$T_L^1 = -\frac{m_1\cdot\psi_L(m_1x_1)\cdot\psi_L'(x_1) - \psi_L'(m_1x_1)\cdot\psi_L(x_1)}{m_1\cdot\chi_L(m_1x_1)\cdot\psi_L'(x_1) - \chi_L'(m_1x_1)\cdot\psi_L(x_1)} \quad \text{(m14)}$$

$$S_L^s = -\frac{\psi_L(m_sx_s)\cdot\left[\psi_L'(x_s)+S_L^{s-1}\chi_L'(x_s)\right] - m_s\cdot\psi_L'(m_sx_s)\cdot\left[\psi_L(x_s)+S_L^{s-1}\chi_L(x_s)\right]}{\chi_L(m_sx_s)\cdot\left[\psi_L'(x_s)+S_L^{s-1}\chi_L'(x_s)\right] - m_s\cdot\chi_L'(m_sx_s)\cdot\left[\psi_L(x_s)+S_L^{s-1}\chi_L(x_s)\right]} \quad \text{(m15)}$$

$$S_L^1 = -\frac{\psi_L(m_1x_1)\cdot\psi_L'(x_1) - m_1\cdot\psi_L'(m_1x_1)\cdot\psi_L(x_1)}{\chi_L(m_1x_1)\cdot\psi_L'(x_1) - m_1\cdot\chi_L'(m_1x_1)\cdot\psi_L(x_1)} \quad \text{(m16)}$$

where E_{Loc} is the electric field originated by the incident radiation, which includes the contribution of all other dipoles:[81]

$$\overline{E}_{Loc}(\overline{r}_j) = \overline{E}_0 \exp(i\overline{k}\cdot\overline{r}_j + i\omega t) - \sum_{l\neq j} \overline{\overline{A}}_{jl}\overline{P}_l \quad \text{(m20)}$$

where $\overline{\overline{A}}_{jl}$ is the interaction matrix. The full expression of $\overline{\overline{A}}_{jl}\overline{P}_l$ is:[81]

$$\overline{\overline{A}}_{jl}\overline{P}_l = \frac{\exp(ik\overline{r}_{jl})}{\overline{r}_{jl}^3} \times \left\{ k^2\overline{r}_{jl}\times(\overline{r}_{jl}\times\overline{P}_l) + \frac{(1-ik\overline{r}_{ij})}{\overline{r}_{jl}^2}\left[\overline{r}_{jl}^2\overline{P}_l - 3\overline{r}_{jl}(\overline{r}_{jl}\cdot\overline{P}_l)\right]\right\} \quad \text{(m21)}$$

An important part of DDA is the use of an appropriate expression for p_i.[81,82] The most applied expression was developed by Draine and Goodman[82] as a correction of the Clausius–Mossotti polarizability by a series expansion of kd and ε_m, where d is the interdipole spacing. This expression was used for our calculations, performed by the software DDSCAT 7.1. More than 10^5 dipoles were used for each target, as required to reduce computational errors well below 10%.[41,81,82] A matrix with the refractive index of 1.334 was used in all cases.

Optical constants

The experimental optical constants of Au, $Au_{84}Fe_{16}$ and $Au_{73}Fe_{27}$ were taken from the literature (ref. 59 and 74) and are reported in Fig. S8.† For all the other values, we used the linear averaging of the optical constants of the two alloys with the closest composition, according to a successful protocol previously published and validated by comparison with experiments.[41,48,54,83]

The optical constants were corrected for size effects,[1,41,84] as reported previously.[41,48,54,84] We adopted a size corrected dielectric constant to account for the intrinsic size effect, which is important when the mean free path of conduction electrons becomes comparable to the particle size l along the direction of polarization promoted by the electromagnetic field. In the assumption that only the free electron behaviour is affected by the size of nanoparticles, $\varepsilon(\omega, l)$ can be expressed in the following way:[1,41,84]

$$\varepsilon(\omega,l) = \varepsilon_\infty(\omega) + \left[\omega_P^2\left(\frac{1}{\omega^2+\Gamma_\infty^2} - \frac{1}{\omega^2+\Gamma(l)^2}\right)\right] + i\left[\frac{\omega_P^2}{\omega}\left(\frac{\Gamma(l)}{\omega^2+\Gamma(l)^2} - \frac{\Gamma_\infty}{\omega^2+\Gamma_\infty^2}\right)\right] \quad \text{(m22)}$$

where $\varepsilon_\infty(\omega)$ is the dielectric function of a bulk metal at the frequency ω, $\Gamma(l)$ is the l-dependent free electron relaxation frequency and Γ_∞ is the bulk metal value. $\Gamma(l)$ is expressed according to a size equation:[1,41,84]

$$\Gamma(l) = \Gamma_\infty + A\frac{v_F}{l} \quad \text{(m23)}$$

where v_F is the electron's Fermi velocity and A is an empirical parameter set equal to 1 in all cases. Eqn (m23) suggests that the damping frequency of NPs with an anistropic shape depends on particle orientation, because l is different for plasmonic oscillations along different directions.[1,41,84] However, what is really important for the right determination of Γ is the ratio A/l and not the value of l. Moreover, the charge distribution of plasmon modes in a nanoparticle does not necessarily coincide with the particle size l along the direction of polarization because, for instance, multipolar modes can also be excited in anisotropic particles.[1] Hence, the simplest choice for present calculations consists in assuming that l is equal to the effective radius of the particle d_{eff}:

$$l = d_{eff} = (3V_{NP}/4\pi)^{1/3} \quad \text{(m24)}$$

where V_{NP} is the particle volume. A similar approximation can also be found in previous studies of other authors.[6,44,85,86] Only in the case of NSs, for the size correction we considered the thickness of the metal shell as the parameter l.[83]

Acknowledgements

Financial support from the University of Padova (PRAT no. CPDA114097/11 and Progetto Strategico STPD11RYPT_001), MIUR (PRIN MULTINANOITA no. 2010JMAZML_001) and "Programma Operativo Nazionale Ricerca e Competitività" 2007–2013, project PAC02L3 00087 SOCIAL-NANO is gratefully acknowledged.

References

1 U. Kreibig and M. Vollmer, *Optical Properties of Metal Clusters*, Springer, Berlin, 1995.
2 G. V. Naik, V. M. Shalaev and A. Boltasseva, *Adv. Mater.*, 2013, **25**, 3264–3294.
3 C. F. Bohren and D. R. Huffman, *Absorption and scattering of light by small particles*, Wiley-Interscience, New York, 1983.
4 F. Borghese, P. Denti and R. Saija, *Scattering from model nonspherical particles: theory and applications to environmental physics*, Springer, 2007.
5 J. R. Cole, N. A. Mirin, M. W. Knight, G. P. Goodrich and N. J. Halas, *J. Phys. Chem. C*, 2009, **113**, 12090–12094.
6 P. K. Jain, K. S. Lee, I. H. El-Sayed and M. A. El-Sayed, *J. Phys. Chem. B*, 2006, **110**, 7238–7248.
7 H. H. Richardson, M. T. Carlson, P. J. Tandler, P. Hernandez and A. O. Govorov, *Nano Lett.*, 2009, **9**, 1139–1146.
8 P. K. Jain, X. Huang, I. H. El-Sayed and M. A. El-Sayed, *Acc. Chem. Res.*, 2008, **41**, 1578–1586.
9 M. B. Cortie and A. M. McDonagh, *Chem. Rev.*, 2011, **111**, 3713–3735.
10 Z. Fang and X. Zhu, *Adv. Mater.*, 2013, **25**, 3840–3856.
11 C. Forestiere, A. J. Pasquale, A. Capretti, G. Miano, A. Tamburrino, S. Y. Lee, B. M. Reinhard and L. Dal Negro, *Nano Lett.*, 2012, **12**, 2037–2044.

12 M. Lester and D. C. Skigin, *J. Opt.*, 2011, **13**, 035105.
13 V. Robbiano, M. Giordano, C. Martella, F. D. Stasio, D. Chiappe, F. B. de Mongeot and D. Comoretto, *Adv. Opt. Mater.*, 2013, **1**, 389–396.
14 N. Lagos, M. Sigalas and E. Lidorikis, *Appl. Phys. Lett.*, 2011, **99**, 063304.
15 V. Amendola and M. Meneghetti, *Adv. Funct. Mater.*, 2012, **22**, 353–360.
16 C. D'Andrea, J. Bochterle, A. Toma, C. Huck, F. Neubrech, E. Messina, B. Fazio, O. M. Marago, E. Di Fabrizio, M. Lamy de La Chapelle, P. G. Gicciardi and A. Pucci, *ACS Nano*, 2013, **7**, 3522–3531.
17 E. Messina, E. Cavallaro, A. Cacciola, R. Saija, F. Borghese, P. Denti, B. Fazio, C. D'Andrea, P. Gucciardi, M. Iati, M. Meneghetti, G. Compagnini, V. Amendola and O. M. Marago, *J. Phys. Chem. C*, 2011, **115**, 5115–5122.
18 B. Metzger, M. Hentschel, T. Schumacher, M. Lippitz, X. Ye, C. B. Murray, B. Knabe, K. Buse and H. Giessen, *Nano Lett.*, 2014, **14**, 2867–2872.
19 A. M. Gobin, M. H. Lee, N. J. Halas, W. D. James, R. A. Drezek and J. L. West, *Nano Lett.*, 2007, **7**, 1929–1934.
20 Y. Wang, K. C. Black, H. Luehmann, W. Li, Y. Zhang, X. Cai, D. Wan, S. Liu, M. Li and P. Kim, *ACS Nano*, 2013, **7**, 2068–2077.
21 R. Huschka, A. Barhoumi, Q. Liu, J. A. Roth, L. Ji and N. J. Halas, *ACS Nano*, 2012, **6**, 7681–7691.
22 J. Huang, K. S. Jackson and C. J. Murphy, *Nano Lett.*, 2012, **12**, 2982–2987.
23 S. Mallidi, T. Larson, J. Aaron, K. Sokolov and S. Emelianov, *Opt. Express*, 2007, **15**, 6583–6588.
24 D. Boyer, P. Tamarat, A. Maali, B. Lounis and M. Orrit, *Science*, 2002, **297**, 1160–1163.
25 C. Leduc, J. Jung, R. R. Carney, F. Stellacci and B. Lounis, *ACS Nano*, 2011, **5**, 2587–2592.
26 B. Lahiri, G. Holland, V. Aksyuk and A. Centrone, *Nano Lett.*, 2013, **13**, 3218–3224.
27 K. Ueno, S. Juodkazis, T. Shibuya, Y. Yokota, V. Mizeikis, K. Sasaki and H. Misawa, *J. Am. Chem. Soc.*, 2008, **130**, 6928–6929.
28 L. Cao, D. N. Barsic, A. R. Guichard and M. L. Brongersma, *Nano Lett.*, 2007, **7**, 3523–3527.
29 A. Urban, M. Fedoruk, M. Horton, J. Radler, F. Stefani and J. Feldmann, *Nano Lett.*, 2009, **9**, 2903–2908.
30 Z. Fang, Y. Zhen, O. Neumann, A. Polman, G. de Abajo, F. Javier, P. Nordlander and N. J. Halas, *Nano Lett.*, 2013, **13**, 1736–1742.
31 O. Neumann, A. S. Urban, J. Day, S. Lal, P. Nordlander and N. J. Halas, *ACS Nano*, 2012, **7**, 42–49.
32 O. Neumann, C. Feronti, A. D. Neumann, A. Dong, K. Schell, B. Lu, E. Kim, M. Quinn, S. Thompson, N. Grady, P. Nordlander, M. Oden and N. J. Halas, *Proc. Natl. Acad. Sci. U. S. A.*, 2013, **110**, 11677–11681.
33 Z. Fang, Y. Wang, Z. Liu, A. Schlather, P. M. Ajayan, F. H. Koppens, P. Nordlander and N. J. Halas, *Acs Nano*, 2012, **6**, 10222–10228.
34 I. Thomann, B. A. Pinaud, Z. Chen, B. M. Clemens, T. F. Jaramillo and M. L. Brongersma, *Nano Lett.*, 2011, **11**, 3440–3446.
35 M. L. Brongersma, N. J. Halas and P. Nordlander, *Nat. Nanotechnol.*, 2015, **10**, 25–34.
36 M. W. Knight, H. Sobhani, P. Nordlander and N. J. Halas, *Science*, 2011, **332**, 702–704.
37 S. Mukherjee, F. Libisch, N. Large, O. Neumann, L. V. Brown, J. Cheng, J. B. Lassiter, E. A. Carter, P. Nordlander and N. J. Halas, *Nano Lett.*, 2012, **13**, 240–247.
38 M. Salmistraro, A. Schwartzberg, W. Bao, L. E. Depero, A. Weber-Bargioni, S. Cabrini and I. Alessandri, *Small*, 2013, **9**, 3301–3307.
39 T. Echtermeyer, L. Britnell, P. Jasnos, A. Lombardo, R. Gorbachev, A. Grigorenko, A. Geim, A. Ferrari and K. Novoselov, *Nat. Commun.*, 2011, **2**, 458.
40 Z. Fang, Z. Liu, Y. Wang, P. M. Ajayan, P. Nordlander and N. J. Halas, *Nano Lett.*, 2012, **12**, 3808–3813.
41 V. Amendola, O. M. Bakr and F. Stellacci, *Plasmonics*, 2010, **5**, 85–97.
42 K. Jiang, D. A. Smith and A. O. Pinchuk, *J. Phys. Chem. C*, 2013, **117**, 27073–27080.
43 G. Baffou, R. Quidant and C. Girard, *Appl. Phys. Lett.*, 2009, **94**, 153109.
44 K. Park, S. Biswas, S. Kanel, D. Nepal and R. A. Vaia, *J. Phys. Chem. C*, 2014, **118**, 5918–5926.
45 M. G. Blaber, M. D. Arnold and M. J. Ford, *J. Phys.: Condens. Matter*, 2010, **22**, 143201.
46 P. K. Jain, K. Manthiram, J. H. Engel, S. L. White, J. A. Faucheaux and A. P. Alivisatos, *Angew. Chem., Int. Ed.*, 2013, **52**, 13671–13675.
47 E. Messina, L. D'Urso, E. Fazio, C. Satriano, M. Donato, C. D'Andrea, O. Maragò, P. Gucciardi, G. Compagnini and F. Neri, *J. Quant. Spectrosc. Radiat. Transfer*, 2012, **113**, 2490–2498.
48 V. Amendola, S. Scaramuzza, S. Agnoli, S. Polizzi and M. Meneghetti, *Nanoscale*, 2014, **6**, 1423–1433.
49 R. Ferrando, J. Jellinek and R. L. Johnston, *Chem. Rev.*, 2008, **108**, 845–910.
50 J. Xiao, S. Fan, F. Wang, L. Sun, X. Zheng and C. Yan, *Nanoscale*, 2014, **6**, 4345–4351.
51 L. Nie, M. Chen, X. Sun, P. Rong, N. Zheng and X. Chen, *Nanoscale*, 2014, **6**, 1271–1276.
52 Y. Yang, J. M. Callahan, T. Kim, A. S. Brown and H. O. Everitt, *Nano Lett.*, 2013, **13**, 2837–2841.
53 M. W. Knight, L. Liu, Y. Wang, L. Brown, S. Mukherjee, N. S. King, H. O. Everitt, P. Nordlander and N. J. Halas, *Nano Lett.*, 2012, **12**, 6000–6004.
54 V. Amendola, M. Meneghetti, O. M. Bakr, P. Riello, S. Polizzi, D. H. Anjum, S. Fiameni, P. Arosio, T. Orlando, C. de Julian Fernandez, F. Pineider, C. Sangregorio and A. Lascialfari, *Nanoscale*, 2013, **5**, 5611–5619.
55 L. Bogani, L. Cavigli, C. de Julián Fernández, P. Mazzoldi, G. Mattei, M. Gurioli, M. Dressel and D. Gatteschi, *Adv. Mater.*, 2010, **22**, 4054–4058.

56 G. Armelles, A. Cebollada, A. Garcia-Martin and M. U. Gonzalez, *Adv. Opt. Mater.*, 2013, **1**, 2–2.
57 S. Sarina, H. Zhu, E. Jaatinen, Q. Xiao, H. Liu, J. Jia, C. Chen and J. Zhao, *J. Am. Chem. Soc.*, 2013, **135**, 5793–5801.
58 J. Suntivich, Z. Xu, C. E. Carlton, J. Kim, B. Han, S. W. Lee, N. Bonnet, N. Marzari, L. F. Allard, H. A. Gasteiger, K. Hamad-Schifferli and Y. Shao-Horn, *J. Am. Chem. Soc.*, 2013, **135**, 7985–7991.
59 Y. Lee, Y. Kudryavtsev, V. Nemoshkalenko, R. Gontarz and J. Rhee, *Phys. Rev. B: Condens. Matter*, 2003, **67**, 104424.
60 S. Lal, S. E. Clare and N. J. Halas, *Acc. Chem. Res.*, 2008, **41**, 1842–1851.
61 Y. Xia, W. Li, C. M. Cobley, J. Chen, X. Xia, Q. Zhang, M. Yang, E. C. Cho and P. K. Brown, *Acc. Chem. Res.*, 2011, **44**, 914–924.
62 M. Choi, R. Bardhan, K. J. Stanton-Maxey, S. Badve, H. Nakshatri, K. M. Stantz, N. Cao, N. J. Halas and S. E. Clare, *Cancer Nanotechnol.*, 2012, **3**, 47–54.
63 D. C. Adler, S. Huang, R. Huber and J. G. Fujimoto, *Opt. Express*, 2008, **16**, 4376–4393.
64 N. Harris, M. J. Ford, P. Mulvaney and M. B. Cortie, *Gold Bull.*, 2008, **41**, 5–14.
65 N. J. Hogan, A. S. Urban, C. Ayala-Orozco, A. Pimpinelli, P. Nordlander and N. J. Halas, *Nano Lett.*, 2014, **14**, 4640–4645.
66 R. Huschka, J. Zuloaga, M. W. Knight, L. V. Brown, P. Nordlander and N. J. Halas, *J. Am. Chem. Soc.*, 2011, **133**, 12247–12255.
67 D. Beaglehole and T. J. Hendrickson, *Phys. Rev. Lett.*, 1969, **22**, 133–136.
68 J. Muñoz, M. Lucas, L. Mauger, I. Halevy, J. Horwath, S. Semiatin, Y. Xiao, P. Chow, M. Stone and D. Abernathy, *Phys. Rev. B: Condens. Matter*, 2013, **87**, 014301.
69 S. Bruzzone and M. Malvaldi, *J. Phys. Chem. C*, 2009, **113**, 15805–15810.
70 M. D. Arnold and M. G. Blaber, *Opt. Express*, 2009, **17**, 3835–3847.
71 G. Baffou, R. Quidant, G. de Abajo and F. Javier, *ACS Nano*, 2010, **4**, 709–716.
72 F. Borghese, P. Denti, G. Toscano and O. I. Sindoni, *J. Math. Phys.*, 1980, **21**, 2754–2755.
73 F. Borghese, P. Denti, R. Saija, G. Toscano and O. I. Sindoni, *Aerosp. Sci. Technol.*, 1984, **3**, 227–235.
74 E. D. Palik, *Handbook of Optical Constants of Solids*, Academic Press, 1985.
75 H. Höchst, P. Steiner and S. Hüfner, *Z. Phys. B: Condens. Matter*, 1980, **38**, 201–209.
76 A. A. Wronkowska and A. Wronkowski, *Vacuum*, 1995, **46**, 469–471.
77 B. Schmidt and D. W. Lynch, *Phys. Rev. B: Condens. Matter*, 1971, **3**, 4015.
78 H. Koike, S. Yamaguchi and T. Hanyu, *J. Phys. Soc. Jpn*, 1976, **40**, 219–225.
79 A. Benhabib, L. Chahed and A. Tadjeddine, *Thin Solid Films*, 1991, **202**, 11–19.
80 M. Blaber, M. Arnold, N. Harris, M. Ford and M. Cortie, *Phys. Rev. B: Condens. Matter*, 2007, **394**, 184–187.
81 P. J. Flatau and B. Draine, *J. Opt. Soc. Am. A*, 1994, **11**, 1491.
82 J. Goodman, B. T. Draine and P. J. Flatau, *Opt. Lett.*, 1991, **16**, 1198–1200.
83 S. Bruzzone, M. Malvaldi, G. Arrighini and C. Guidotti, *J. Phys. Chem. B*, 2006, **110**, 11050–11054.
84 V. Amendola and M. Meneghetti, *J. Phys. Chem. C*, 2009, **113**, 4277–4285.
85 C. Noguez, *J. Phys. Chem. C*, 2007, **111**, 3806–3819.
86 C. Noguez, *Opt. Mater.*, 2005, **27**, 1204–1211.

